

Neural Vector Fields: Generalizing Distance Vector Fields by Codebooks and Zero-Curl Regularization

Xianghui Yang, Guosheng Lin *Member, IEEE*, Zhenghao Chen, Luping Zhou *Senior Member, IEEE*

arXiv:2309.01512v1 [cs.CV] 4 Sep 2023

Abstract—Recent neural networks based surface reconstruction can be roughly divided into two categories, one warping templates explicitly and the other representing 3D surfaces implicitly. To enjoy the advantages of both, we propose a novel 3D representation, Neural Vector Fields (NVF), which adopts the explicit learning process to manipulate meshes and implicit unsigned distance function (UDF) representation to break the barriers in resolution and topology. This is achieved by directly predicting the displacements from surface queries and modeling shapes as Vector Fields, rather than relying on network differentiation to obtain direction fields as most existing UDF-based methods do. In this way, our approach is capable of encoding both the distance and the direction fields so that the calculation of direction fields is differentiation-free, circumventing the non-trivial surface extraction step. Furthermore, building upon NVFs, we propose to incorporate two types of shape codebooks, *i.e.*, NVFs (Lite or Ultra), to promote cross-category reconstruction through encoding cross-object priors. Moreover, we propose a new regularization based on analyzing the zero-curl property of NVFs, and implement this through the fully differentiable framework of our NVF (ultra). We evaluate both NVFs on four surface reconstruction scenarios, including watertight vs non-watertight shapes, category-agnostic reconstruction vs category-unseen reconstruction, category-specific, and cross-domain reconstruction.

Index Terms—Surface Reconstruction, Point Clouds, Mesh, Generalization, Codebook, Curl.

1 INTRODUCTION

RECONSTRUCTING continuous surfaces is a challenging yet emerging task in various machine-vision applications [5], [7], [38], [43] as unstructured, discrete, and sparse point clouds are hard to be deployed into the downstream applications. The remarkable success of Deep Neural Networks (DNNs) has led to the rapid development of several learning-based surface reconstruction methods. These methods can be categorized into **explicit** or **implicit** representation methods.

For explicit representation methods, they warp templates [3], [4], [19], [26], [29], [70] or predict voxel grids [10], [30], [60], [61] to provide explicit representations, which are friendly to human perception and downstream applications

- Xianghui Yang, Zhenghao Chen and Luping Zhou are with the School of Electrical and Information Engineering, The University of Sydney, Sydney, NSW 2006, Australia (e-mail: luping.zhou@sydney.edu.au).
- Guosheng Lin is with the School of Computer Science and Engineering, Nanyang Technological University, Singapore 639798.

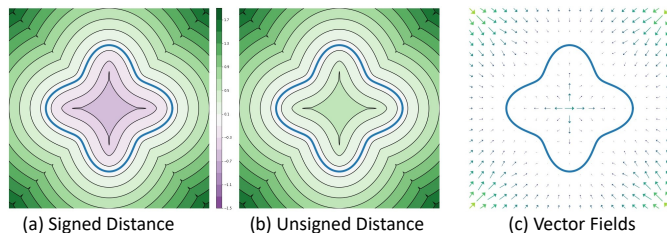


Fig. 1: Implicit surface representation methods for watertight shapes: (a) signed distance functions, (b) unsigned distance functions, and (c) our proposed approach vector fields. The blue line indicates the depicted shape.

(*e.g.*, editing and rendering). However, these explicit methods are usually limited by topology and resolution.

On the other hand, implicit representation methods have recently garnered more attention due to their ability to represent surfaces with arbitrary topology, in contrast to explicit methods. Early methods, [12], [14], [22], [35], [40], [45], [49] predict the query point as occupancy values or signed distance and then represent the surface as an isocontour of a scalar function as shown in Fig. 1a, while generally require specific preprocessing to close non-watertight meshes and remove inner structures. Recently, Unsigned Distance Functions (UDFs) [15], [79] are introduced to overcome the high computational preprocessing that eliminates internal structures in the early methods using signed distance functions (SDFs), as shown in Fig. 1b. Despite certain advantages, UDFs require a more complicated surface extraction process (Ball-Pivoting Algorithm [5] or gradient-based Marching Cube [28], [89]) which relies on model differentiation during inference (*i.e.*, differentiation-dependent).

In this work, we propose Neural Vector Fields (NVFs), encompassing the “lite” and “ultra” versions, to leverage the advantages of both the direct manipulation processes from the explicit learning strategy and the powerful representation ability for complex continuous surfaces from the implicit functions for 3D surface reconstruction. Our NVF model the 3D shapes as vector fields and learns a function measuring the displacements of query points to their nearest-neighbor points on the 3D surface. The displacement output of the function could be used directly to deform the source meshes. Therefore, NVFs could serve

both as an implicit function and an explicit deformation. Our NVF not only benefits from the advantages of both explicit and implicit representations but also overcomes their drawbacks. Firstly, NVF representation avoids the comprehensive inference process by skipping the gradient calculation during the surface extraction procedure¹ through directly learning displacement. Such a one-pass forward-propagation nature frees NVF from differentiation dependency and significantly reduces the inference time and memory cost. Secondly, NVFs provide more flexibility to incorporate modules, such as shape codebooks, to promote cross-category surface reconstruction and improve model generalization. Although implicit functions have certain advantages, they often lack the ability to generalize due to their tendency to overfit. We therefore propose to encode cross-category shape priors in two types of shape codebooks. This first one is a hard codebook, dubbed NVF (lite), which consists of un-differentiable discrete shape codes in the embedded feature space using the Vector Quantization (VQ) strategy. As it cuts off gradients, its incorporation with conventional UDFs is retarded as the latter requires gradient information for surface extraction. In contrast, the hard codebook could be seamlessly integrated with NVFs representation thanks to its differentiation-free nature. Such an integration not only improves model generalization but also accelerates the training procedure as a regularization term. Moreover, we further propose a “soft” codebook with the cross-attention mechanism, dubbed NVF (ultra). Compared with the “hard” codebook that relies on the non-differentiable operation of the nearest search for encoding, our NVF (ultra) leverages the multi-head cross-attention mechanism to combine code items for encoding. This significantly enlarges the space of representation, as well as the perception fields by considering all possible code items in the codebook at the cost of memory. Meanwhile, our soft codebook enables a fully differentiable encoding process, allowing us to jointly optimize the framework and other potential constraints in an end-to-end manner to improve the reconstruction performance.

On top of the end-to-end design in NVF (ultra), we could further apply zero-curl theory and direction loss as two additional constraints to jointly supervise the point offsets to the surface. It is noted that both the gradient fields of SDF, UDF and the distance vector field of NVF are conservative vector fields and should theoretically satisfy the property of zero curl. Therefore, we propose a curl regularization to avoid circular vector fields that will result in inaccurate gradients/displacements, leaving uneven surfaces and little holes after surface extraction if the circulations happen near the surface. That is, the divergence of the field should be negative and the curl of the field should be zero (*i.e.*, $\nabla \cdot \mathbf{v} < 0$ & $\nabla \times \mathbf{v} = \mathbf{0}$, \mathbf{v} denotes any vector within the fields). To implement curl regularization, we obtain the Jacobian matrix by respectively calculating the first-order partial derivatives of the predicted displacements along x , y , and z directions, followed by computing the curl of distance vector fields and minimizing it to the zero-curl fields.

1. Learning-based methods calculate the gradients of distance fields through model differentiation. The opposite direction of the gradients should point to the nearest-neighbor point on the target surface.

In addition to zero-curl regularisation, we also propose a direction loss to maximize the cosine similarity between the predicted and ground-truth displacements to further surface smoothness.

We conducted extensive experiments on two benchmark reconstruction datasets, which are the synthetic dataset ShapeNet [8] and the real scanned dataset MGN [6]. We perform our algorithm with other methods in four tasks: category-specific, category-agnostic, category-unseen, and cross-domain reconstruction tasks. The results demonstrate that our NVF (ultra) framework achieves state-of-the-art reconstruction results in nearly all tasks and all metrics.

Our contributions are summarized as follows.

- We propose NVF for better 3D field representation, which bridges the explicit learning and implicit representations, and benefits from both of their advantages. Our method can obtain the displacement of a query location in a differentiation-free way, and thus it significantly reduces the inference complexity and provides more flexibility in designing network structures which may include non-differentiable components.
- On top of NVF, we propose to learn shape codebooks, either “hard” or “soft” to encode shape priors to improve model generalization and cross-category reconstruction. The “hard” codebook encodes each query location as a composition of discrete codes in feature space, while the soft one incorporates all coded items via a cross-attention mechanism. The former is computationally less complex, while the latter, although at the cost of increased use of memory, has more flexibility of representation and allows end-to-end optimization with a fully differentiable encoding process.
- We propose two new constraints: curl regularization and direction loss to improve surface quality and prevent large holes by calculating the Jacobian matrix and enforcing zero-curl fields.
- We conducted extensive experiments to evaluate the effectiveness of our proposed method. The results demonstrate consistent and promising performance on two benchmarks across various evaluation scenarios.

Our preliminary work has been published in a conference paper [76]. This manuscript is a substantial extension of our previous investigation in the following ways. First, we extend the hard codebook used in [76] to a soft codebook by incorporating all coded items through a cross-attention mechanism. This not only boosts model generalization with more flexibility of encoding shape priors, but also allows end-to-end optimization with a fully differentiable encoding process. Second, this extended study incorporates a comprehensive analysis of the zero-curl and negative divergence properties of the distance vector fields, offering additional regularizations (curl regularization and direction loss) for field learning. Third, we redo all the experiments on different reconstruction scenarios for our newly proposed soft codebook and regularizations. The culmination of our preliminary research and these novel extensions establish a robust foundation for the advancement of surface reconstruction and ultimately yield state-of-the-art results in surface reconstruction with improved generalization.

2 RELATED WORK

2.1 Explicit Representations

Voxels [17], [44], [59] served as the early shape representation method, which can be discretized into grids and processed by subsequent deep learning processing techniques [34], [37], [54], [71], [72]. However, memory footprint usually makes such methods computationally expensive for high-resolution applications and it is non-trivial to reduce such computational costs [10], [30], [55], [58], [61]

In contrast, point cloud approaches offer a more efficient means of representing surfaces. Recent learning-based point cloud processing methods [9], [50], [62], [69], [87] have achieved remarkable success in 3D shape analysis [16], [32], [33], [42], [68], [83], [90] and synthesis [1], [26], [78], [82]. Nevertheless, point clouds often fail to provide detailed geometric information, thereby limiting their usefulness in downstream applications.

In order to incorporate rich geometry information (*e.g.*, surfaces and topology), 3D shapes can be represented as polygonal meshes [36], [41], [51], [67], [77]. However, traditional polygonal meshes are often characterized by fixed topology, as they deform a predefined template such as sphere [36], [47], [77]) into desired shapes by manipulating vertices, which requires non-trivial processes [25], [26], [47] to alleviate.

In general, distance vector fields offer a distinct advantage over explicit methods, as they rely on explicit deformations using vector fields for learning purposes. This approach effectively circumvents the limitations imposed by the fixed topology and resolution of the templates, allowing greater flexibility in the modeling process.

2.2 Implicit Representations

Implicit representation can overcome the limitations of limited resolution and fixed mesh topology by representing continuous surfaces. These methods typically employ multi-layer perceptions (MLPs) to generate binary occupancy [14], [18], [24], [45], [56], [57] or signed distance functions (SDFs) [12], [35], [48] based on spatial locations. However, they require extensive pre-processing to artificially close the surfaces and obtain watertight meshes, and lack generalization on non-watertight ones. In order to address the above issues, Chibane *et al.* [15] introduced unsigned distance functions (UDFs) to learn the unsigned distance, while subsequent methods [64], [66], [76], [79], [86], [89] are also introduced to improve the performance and generalization of UDFs. For instance, GIFS [79] utilizes an intersection classification branch and CAP-UDF [89] optimizes models directly on raw point clouds. Although these UDF-based methods can improve the generalization of implicit representation, they require expensive surface extraction processing [5], [28], [89]. Recently, Yang *et al.* [76] proposed distance vector fields (DVF) that encode both distance and direction fields, freeing surface extraction from differentiation. However, it adopts a vector quantization strategy with a “hard” codebook design to encode cross-object priors, while non-differentiable operation retards the framework to jointly optimize with other constraints (*e.g.*, curl regularization) in an end-to-end manner. Our proposed method, NVF (ultra), replaces the “hard” codebook with a

fully-differentiable soft codebook, which not only enhance model generalization but also enable the framework to jointly optimize with essential regularization terms.

2.3 Codebook

The vector quantization (VQ) is introduced to discretize and compress extracted features into compact representations (*i.e.*, codebook), which was first proposed by Oord *et al.* in the VQ-VAE [63]. Subsequently, Yu *et al.* developed the VQ-GAN [81], which utilizes codebooks with adversarial learning for generating high-quality images. Since then, numerous methods have adopted this strategy for various applications such as image generation [21], [27], [39], [52], speech synthesis [20], [75], video processing [23], [31], [53], [65], compression [2], [11], and the realm of 3D fields [13], [46], [74], [84]. Despite the tremendous success, the major limitation is that it cannot support end-to-end differentiability, as it only replaces the query with the closest code, thereby halting gradient flow. Recently, attention mechanisms have been introduced to make use of all codes in the codebook and improve performance for the corresponding tasks [80], [85], [88]. Our work not only introduces such a “soft” codebook to enhance feature representation but also leverages this differentiable non-local operation to achieve end-to-end differentiability so that we can further incorporate other constraints (*e.g.*, curl regularization) and jointly optimize them in our framework.

3 METHODOLOGY

Our objective is to reconstruct the original surface \mathcal{S} from a sparse point cloud $P \in \mathbb{R}^{N \times 3}$ using distance vector fields (DVF) as a representation. These DVFs predict displacement vectors $\mathbf{v} \in \mathbb{R}^3$ that move the point \mathbf{q} to the closest points $\hat{\mathbf{q}}$ on the underlying surface. Our framework consists of three key components, namely, Feature Extraction, Codebook, and Field Prediction, as depicted in Fig. 2. In particular, for optimizing Field Prediction, we adopt a curl regularization and direction loss as additional constraints. The details of each module are further elaborated below.

3.1 Distance Vector Fields

Our NVF (lite and ultra) both adopt a neural network function, which models the underlying shape \mathcal{S} by predicting the field of displacements \mathbf{v} for each given query point $\mathbf{q} \in Q$ to its nearest point $\hat{\mathbf{q}} \in \mathcal{S}$ on the surface. The formulation of this method is given by:

$$\text{NVF}(\mathbf{q}) = \mathbf{v} = \min_{\hat{\mathbf{q}} \in \mathcal{S}} \hat{\mathbf{q}} - \mathbf{q}. \quad (1)$$

In general, we produce vector fields as directional distance fields as in [76], which encode both distance and directional fields $d = \|\hat{\mathbf{q}} - \mathbf{q}\|_2$ and $\mathbf{g} = (\hat{\mathbf{q}} - \mathbf{q}) / \|\hat{\mathbf{q}} - \mathbf{q}\|_2$.

3.2 Feature Extraction

Though many existing backbones [9], [50], [87] could be used as the feature encoder, for simplicity, we directly adopt the feature extraction module in NVF [76] to extract 3D shape features f_i for each point \mathbf{p}_i from the point cloud P and produce the feature embedding z for a given query

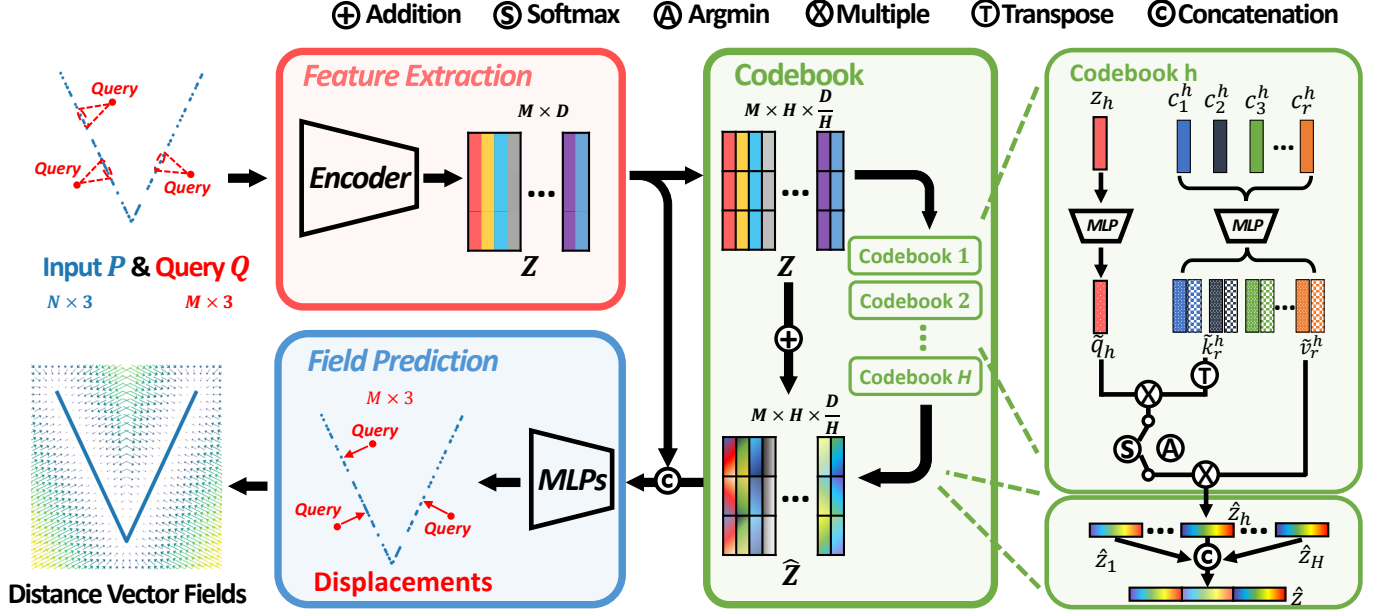


Fig. 2: Overview of our NVF (lite and ultra) framework. If the codebook is switched to the \textcircled{S} mode, the NVF (ultra) will be activated via a softmax operation; if the codebook is switched to the \textcircled{A} mode, the NVF (lite) mode will be activated through an argmin operation. Our model encodes the input point cloud (blue dots), samples features for each query point (red dots), and fuses query embeddings via either a hard (NVF (lite)) or a soft (NVF (ultra)) codebook to predict the displacements of query location to the target surface (red arrow).

point \mathbf{q} by concatenating K signatures z_i ($i = 1, \dots, K$), that is, $z = \text{Concat}(z_1, z_2, \dots, z_i, \dots, z_K)$. Each signature z_i is obtained by nonlinearly transforming a quadruple consisting of the 3D position of \mathbf{q} , the 3D positions of \mathbf{q} 's K nearest points \mathbf{p}_i on the point cloud P , the displacement of \mathbf{q} to \mathbf{p}_i , and the feature f_i of \mathbf{p}_i . Mathematically, the signature z_i can be represented by $z_i = \text{MLP}(\mathbf{q}, \mathbf{p}_i, \mathbf{p}_i - \mathbf{q}, f_i)$, $i = 1, 2, \dots, K$.

3.3 Codebook

A multi-head codebook $\mathcal{C} \in \mathbb{R}^{H \times R \times \frac{D}{H}}$ is learned to extract cross-object priors, while the ‘‘soft’’ codebook enhances the representation ability of the ‘‘hard’’ codebook used in NVF by using a larger search space for encoding. Here D , H and R represent the dimension of the embedding z , the number of the sub-codebooks (*i.e.*, heads), and the number of discrete codes c_r ($r = 1, \dots, R$) within each sub-codebook. The dimension of each discrete code is $\frac{D}{H}$.

Hard Codebook. We divide the continuous embedding z_q into H segments along the channel dimension. Each segment is denoted as z_q^h . To obtain discrete representations, we find the nearest code in the corresponding sub-codebook \mathcal{C}^h for each segment z_q^h , using the Euclidean distance as a measure. This discretization process results in the creation of \hat{z}_q , which is composed of discrete segment codes that represent the original continuous embedding z_q . This process can be formulated as follows,

$$\begin{aligned} z_q &= z_q^1 \oplus z_q^2 \oplus \dots \oplus z_q^h \oplus \dots \oplus z_q^H, \\ \hat{z}_q &= c_{r_1^*}^1 \oplus c_{r_2^*}^2 \oplus \dots \oplus c_{r_h^*}^h \oplus \dots \oplus c_{r_H^*}^H, \\ r_h^* &= \arg \min_{r \in \{1, \dots, R\}} \|z_q^h - c_r^h\|_2. \end{aligned} \quad (2)$$

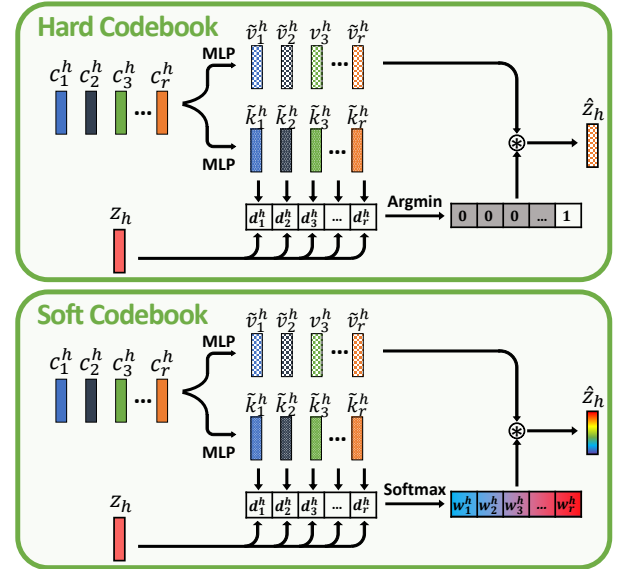


Fig. 3: Overview of our proposed hard and soft codebook mechanisms. The hard codebook updates the feature z_h by sampling its nearest code with an argmin operation, whereas the soft codebook updates the feature z_h by combining all codes based on learned similarity values with a softmax function.

When using a single codebook $\mathcal{C} \in \mathbb{R}^{(HR) \times D}$, the feature space is limited in size and lacks diversity. Differently, by adopting a multi-head codebook, R^H permutations are introduced, effectively expanding the feature space from \mathbb{R}^{HR} to \mathbb{R}^{R^H} . This augmentation significantly enhances the representation capacity. Meanwhile, it's important to

be aware that the nearest search operation at this stage interrupts the gradient flow. Despite this, the multi-head codebook can still be jointly learned during training. This is achieved by minimizing the distance between the continuous embedding z and its discretization \hat{z}_q , which can be formulated as follows:

$$\mathcal{L}_{code} = \sum_{h \in \{1, \dots, H\}} \|sg(c_{r_h^*}^h) - z_q^h\|_2^2 + \beta \|sg(z_q^h) - c_{r_h^*}^h\|_2^2, \quad (3)$$

where the ‘‘stop gradient’’ operation defined by sg and the weight β for the commitment loss in the second term. Additionally, it proposes an alternative approach to update the discretized embedding \hat{z}_q and its corresponding codes ($\hat{z}_q^h \equiv c_{r_h^*}^h$) in the codebook using the *Exponential Moving Average* [63]:

$$c_{r_h^*}^h := \gamma c_{r_h^*}^h + (1 - \gamma) z_q^h, \quad (4)$$

with γ is a value between 0 and 1.

Soft Codebook. To encode the feature embedding z of the query point \mathbf{q} using the multi-head codebook, we first split the continuous embedding z into H segments along the channel dimension, corresponding to the H sub-codebooks. Each segment of the embedding, denoted as z^h ($h = 1, \dots, H$), is then transformed by MLP into a vector known as *Query* \tilde{q}^h , while at the same time, each discrete code c_r^h ($r = 1, \dots, R$) in the corresponding h -th sub-codebook is also transformed by MLP to form the vectors *Key* \tilde{k}_r^h and *Value* \tilde{v}_r^h , respectively. The three vectors \tilde{q}^h , \tilde{k}_r^h , and \tilde{v}_r^h are then used to encode z^h by \hat{z}^h through their cross-attention defined in Eq. (5).

$$\begin{aligned} z &= z^1 \oplus z^2 \oplus \dots \oplus z^h \dots \oplus z^H, \\ \hat{z} &= \hat{z}^1 \oplus \hat{z}^2 \oplus \dots \oplus \hat{z}^h \dots \oplus \hat{z}^H, \\ \tilde{q}^h, \tilde{k}_r^h, \tilde{v}_r^h &= MLP_q(z^h), MLP_k(c_r^h), MLP_v(c_r^h) \quad (5) \\ \hat{z}^h &= \sum_{r=1}^R softmax\left(\frac{\tilde{q}^h \tilde{k}_r^h}{\sqrt{d_k}}\right) \tilde{v}_r^h \end{aligned}$$

Here, $d_k = D/H$ is the code dimension and the symbol \oplus denotes concatenation. As can be seen, now \hat{z}^h is encoded by the linear combination of \tilde{v}_r^h which is transformed from the codes c_r^h in the codebook. Compared with the discrete encoding in the vanilla codebook used by NVF, \hat{z}^h is now a continuous variable, which significantly increases the space of representation and therefore, further enhances the generalization capacity. Meanwhile, the fully-differentiable cross-attention operation enables our framework to train in an end-to-end manner. The codes stored in the codebook are learnable parameters that can be jointly learned by optimizing final losses in Sec. 3.6, different from NVF which optimizes an additional loss function to learn the codebook.

3.4 Field Prediction

We take the continuous embedding z and its discretization \hat{z} to predict a vector as the displacement for the query point \mathbf{q} to move to the ground truth surface \mathcal{S} . By combining the embeddings z and \hat{z} , the final vector field is predicted using MLPs, *i.e.*, $NVF(\mathbf{q}) = MLPs(z, \hat{z})$.

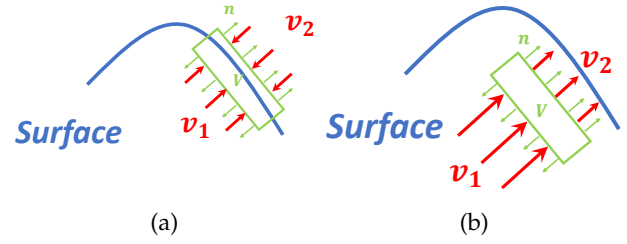


Fig. 4: Illustration of negative divergence condition in a distance vector field. (a) The volume includes the underlying surface, and the vectors are opposite to the surface normals of the volume. (b) The volume does not include the underlying surface, and the magnitude of vectors opposite to surface normals is larger than vectors oriented along with surface normals of the volume. These two scenarios both correspond to negative divergence (*i.e.*, $\nabla \cdot \mathbf{v} < 0$).

3.5 Curl and Divergence

In theoretical terms, distance vector fields are required to satisfy the active and irrotational conditions, implying that the divergence of the field should be negative ($\nabla \cdot \mathbf{v} < 0$), and the curl of the field should equal zero ($\nabla \times \mathbf{v} = \mathbf{0}$). Thus we employ these two operators on the DVFs to depict their active and rotational properties and impose curl regulation during the learning process. Before explaining how to use the curl regularization, we need to establish why the DVFs conform to these conditions. In vector calculus, the curl is a vector operator that characterizes the infinitesimal circulation of a vector field in three-dimensional Euclidean space, while the divergence is a vector operator that performs on a vector field, creating a scalar field indicating the quantity of the vector field’s source at each point. These operators describe the outward flux and circulation density of vector fields. We give the following theorem.

Theorem 3.1. *Given a distance vector field $\mathbf{v}(x, y, z)$ such that $\mathbf{v}(x, y, z) = -\phi \nabla \phi$, where $\phi(\cdot)$ denotes an unsigned distance field whose gradient is $\nabla \phi$, it can be shown that the distance vector field $\mathbf{v}(x, y, z)$ is an irrotational field and satisfies zero-curl condition $\nabla \times \mathbf{v} = \mathbf{0}$.*

Proof. For a distance vector field $\mathbf{v}(x, y, z) = -\phi \nabla \phi$, where $\phi(\cdot)$ denotes an unsigned distance field whose gradient is $\nabla \phi$, it can be written as the gradient of the potential function $-\frac{1}{2} \phi^2(x, y, z)$, which is a scalar function. That is,

$$\mathbf{v} = \nabla\left(-\frac{1}{2} \phi^2\right) = -\phi \nabla \phi. \quad (6)$$

Therefore, the distance vector field $\mathbf{v}(x, y, z)$ is indeed a **conservative** vector field. For any **conservative** vector field, it is an irrotational vector field and thus $\mathbf{v}(x, y, z)$ eventually forms a zero-curl field. \square

Intuitively, the magnitude and the direction of the vector field \mathbf{v} are determined by the unsigned distance function $\phi(x, y, z)$ and its gradient $\nabla \phi(x, y, z)$, respectively. It is mathematically formulated as $\mathbf{v}(x, y, z) = -\phi \nabla \phi$. According to Theorem 3.1, it is an irrotational vector field and thus should form a zero-curl field.

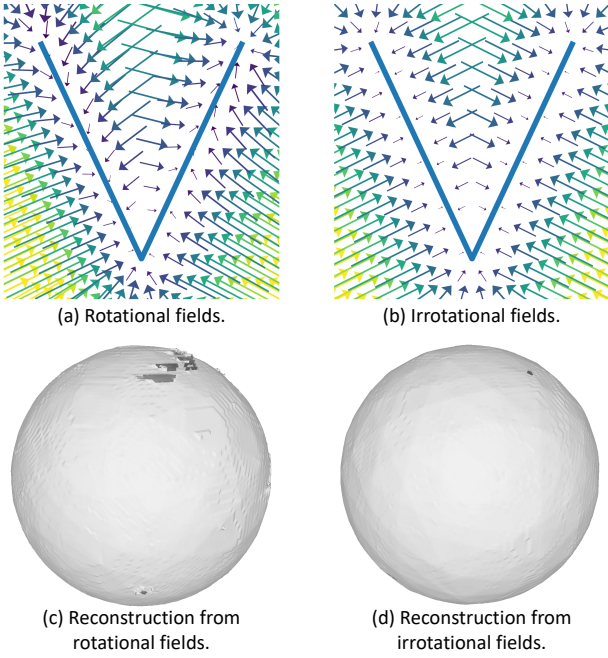


Fig. 5: (a) Rotational distance vector fields. (b) Irrotational distance vector fields with zero curl (*i.e.*, $\nabla \times \mathbf{v} = \mathbf{0}$). Reconstruction examples from rotational fields and irrotational fields, where the DVF fits the scene containing a simple sphere (c) with curl or (d) w/o curl regularization. The comparison between (c) and (d) demonstrates that the inaccurate direction of vectors would mislead the surface reconstruction (*e.g.*, leaving holes, and uneven surfaces) as the surface extraction process from distance vector fields relies on the gradient-based marching cubing operation.

Theorem 3.2. Given a distance vector field $\mathbf{v}(x, y, z) = -\phi\nabla\phi$, it can be shown that $\mathbf{v}(x, y, z)$ is an active field and satisfies the negative divergence condition $\nabla \cdot \mathbf{v} < 0$.

Proof. The divergence of a distance vector field $\mathbf{v}(x, y, z) = -\phi\nabla\phi$ at any 3D point \mathbf{x} is defined as the ratio limit of the surface integral of $\mathbf{v}(\mathbf{x})$ out of the closed surface of volume V , which encloses the given point \mathbf{x} , as V shrinks to zero. This can be formulated as,

$$\nabla \cdot \mathbf{v} = \lim_{V \rightarrow 0} \frac{1}{|V|} \iint_{S(V)} \mathbf{v} \cdot \mathbf{n} dS. \quad (7)$$

$|V|$ and $S(V)$ are the volume and the boundary of V . \mathbf{n} is the outward unit normal to that surface of V .

Assuming the volume includes the underlying surface as shown in Fig. 4a, the distance vectors at the boundary $S(V)$ point inward, in opposition to the surface normals of the closed volume, which yields $\mathbf{v} \cdot \mathbf{n} < 0$ and results in the integral in Eq. (7) negative.

In contrast, assuming the volume does not include the underlying surface as shown in Fig. 4b, the magnitude of vectors on the closer side to the target shape (*i.e.*, \mathbf{v}_2 in Fig. 4b) is less than that of on the far side (*i.e.*, \mathbf{v}_1 in Fig. 4b), which implies $\|\mathbf{v}_2\|_2 < \|\mathbf{v}_1\|_2$. Since $\mathbf{v}_1 \cdot \mathbf{n} < 0$ and $\mathbf{v}_2 \cdot \mathbf{n} > 0$, we will have $\mathbf{v}_1 \cdot \mathbf{n} + \mathbf{v}_2 \cdot \mathbf{n} < 0$. Therefore, the integral in Eq. (7) is also negative. \square

Theorem 3.2 shows that the divergence of the distance vector field $\mathbf{v}(x, y, z)$ is negative (*i.e.*, $\nabla \cdot \mathbf{v} < 0$). Note that, although we show $\mathbf{v}(x, y, z)$ is an active field, we did not use the negative divergence condition to regularize our reconstruction due to its complexity for optimization. This could be further explored in our future work.

In addition, we present an example to visualize the rotational and irrotational fields in Fig. 5(a,b), with particular emphasis on their behavior near the object. For better comparison, we employ a 4-layer MLP model to fit a sphere under L1 supervision to facilitate an equitable comparison of the reconstructed results from both using and without using curl regularization, as depicted in Fig. 5(c,d). The reconstructed surfaces affirm the efficacy of incorporating curl regularization for achieving smoothness and bridging small gaps in the resulting surfaces.

It is important to note that the active property has already been taken into account in the existing learning process, as the primary objective is to fit a distance field, and the distance loss can serve as divergence regularization. However, to ensure that the model conforms to the irrotational property, additional measures need to be taken. The properties mentioned above are present exclusively in differentiable regions since they are also non-differentiable areas. A non-curl DVF is shown in Fig. 5. It has been established that distance vector fields satisfying the zero-curl and negative divergence conditions are ideal, and it is desirable to incorporate these properties into the optimization process.

Assuming the predicted offsets composed of elements on three axes are $\mathbf{v} = (v_x, v_y, v_z)$, where v_x, v_y, v_z are functions of position (x, y, z) . The curl operator on the distance vector fields can be formulated as,

$$\begin{aligned} \nabla \times \mathbf{v} &= \begin{bmatrix} \mathbf{i} & \mathbf{j} & \mathbf{k} \\ \frac{\partial}{\partial x} & \frac{\partial}{\partial y} & \frac{\partial}{\partial z} \\ v_x & v_y & v_z \end{bmatrix} \\ &= \left(\frac{\partial v_z}{\partial y} - \frac{\partial v_y}{\partial z} \right) \mathbf{i} + \left(\frac{\partial v_x}{\partial z} - \frac{\partial v_z}{\partial x} \right) \mathbf{j} + \left(\frac{\partial v_y}{\partial x} - \frac{\partial v_x}{\partial y} \right) \mathbf{k} \\ &= \mathbf{0} \end{aligned} \quad (8)$$

where $\mathbf{i}, \mathbf{j}, \mathbf{k}$ are unit vectors along the x -, y -, and z -axes, respectively. It is observed that enforcing the curl of the field to be zero is equivalent to forcing their components to be zero, defined as,

$$\frac{\partial v_z}{\partial y} = \frac{\partial v_y}{\partial z}, \quad \frac{\partial v_x}{\partial z} = \frac{\partial v_z}{\partial x}, \quad \frac{\partial v_y}{\partial x} = \frac{\partial v_x}{\partial y} \quad (9)$$

To obtain the first-order partial derivatives in Eq. (9), we must calculate the Jacobian matrix which can be defined as,

$$\mathbf{J}(\mathbf{v}) = \begin{bmatrix} \frac{\partial v_x}{\partial x} & \frac{\partial v_x}{\partial y} & \frac{\partial v_x}{\partial z} \\ \frac{\partial v_y}{\partial x} & \frac{\partial v_y}{\partial y} & \frac{\partial v_y}{\partial z} \\ \frac{\partial v_z}{\partial x} & \frac{\partial v_z}{\partial y} & \frac{\partial v_z}{\partial z} \end{bmatrix} \quad (10)$$

It is observed that encouraging the curl of the field to be zero is equivariant to encouraging the Jacobian matrix to be a symmetry matrix. The curl regularization is,

$$\mathcal{L}_{curl} = \|\mathbf{J}(\mathbf{v}) - \mathbf{J}(\mathbf{v})^T\|_F \quad (11)$$

where $\|\cdot\|_F$ denotes Frobenius Norm and it is defined as the square root of the sum of the absolute squares of its elements, *e.g.*, $\|A\|_F = \sqrt{\sum_i \sum_j |a_{ij}|^2}$, $A \in \mathcal{R}^{m \times n}$.

3.6 Optimization.

Lite. To optimize NVF (lite), we focus on minimizing both the predicted displacement $\Delta \mathbf{q}$ and the discrepancy with the ground-truth displacement $\hat{\mathbf{q}} - \mathbf{q}$. Additionally, we consider the discretization error of the continuous embedding z_q as it transitions into \hat{z}_q . In order to prevent gradient flow beyond vector quantization, we utilize the “stop-gradient” operation (sg). The comprehensive objective function can be expressed as follows:

$$\mathcal{L} = \sum_{\mathbf{q} \in \mathcal{Q}} \|\hat{\mathbf{q}} - \mathbf{q} - \Delta \mathbf{q}\|_1 + \lambda \sum \|z_q - sg(\hat{z}_q)\|_2^2. \quad (12)$$

We use a hyper-parameter the parameter λ to determine the balance between the two loss terms. The commitment loss term $\|sg(z) - z^q\|_2^2$ in Equation 3 has been replaced with the *Exponential Moving Average* algorithm. This replacement is applied to update the corresponding codes in the multi-head codebook.

Ultra We optimize NVF (ultra) by minimizing the difference between the predicted displacement \mathbf{v} and the ground-truth displacement $\hat{\mathbf{q}} - \mathbf{q}$, curl regularization \mathcal{L}_{curl} , and the direction loss \mathcal{L}_{dir} measuring the directional error of \mathbf{v} and $\hat{\mathbf{q}} - \mathbf{q}$. In sum, our overall objective function is as follows.

$$\mathcal{L} = \mathcal{L}_{l_1} + \lambda_{curl} \mathcal{L}_{curl} + \lambda_{dir} \mathcal{L}_{dir} \quad (13)$$

where $\mathcal{L}_{l_1} = \|\mathbf{v} - (\hat{\mathbf{q}} - \mathbf{q})\|_1$ and $\mathcal{L}_{dir} = 1 - \frac{\mathbf{v} \cdot (\hat{\mathbf{q}} - \mathbf{q})}{\|\mathbf{v}\|_2 \|\hat{\mathbf{q}} - \mathbf{q}\|_2}$. The hyperparameters λ_{curl} and λ_{dir} balance the loss magnitude.

3.7 Surface Extraction

Both signed and unsigned distance functions define the surfaces as a 0-level set. SDFs extract surfaces through Marching Cubes [43] faithfully due to the intersection being easily captured via sign flipping. Recently, MeshUDF [28] and CAP-UDF [89] propose to detect the opposite gradient directions to replace the sign in SDFs and successfully apply the Marching Cubes [43] on UDFs. Note that these two methods learn distance fields and they need to differentiate the distance field to obtain the gradient direction. In contrast, our NVF can similarly extract surfaces using Marching Cubes while avoiding the differentiation of the distance field. This is because our NVF directly encodes both distance and direction fields. The surface extraction algorithm divides the space into grids and decides whether the adjacent corners are located on the same side or two sides. NVF predicts the vectors $\Delta \mathbf{q}$ of all lattices and normalizes them into normal vectors $\mathbf{g}_i = \Delta \mathbf{q}_i / \|\Delta \mathbf{q}_i\|_2$. Given a lattice gradient \mathbf{g}_i and its adjacent lattices’ gradients \mathbf{g}_j , the algorithm checks if their gradients have opposite orientations, and assigns the pseudo sign s_i to the lattice. For more details, please refer to MeshUDF [28].

4 EXPERIMENTS

4.1 Experimental Protocol

Lite and Ultra. When considering the usage of the soft codebook and training with curl and direction loss, it is important to acknowledge the significant increase in memory requirements and time consumption. In light of these factors, we have designated this approach as NVF (ultra). In contrast, the employment of a hard codebook involves

sampling the closest code based on Euclidean distance. While this method is not compatible with curl loss, it only necessitates a minimal additional memory allocation. Consequently, we refer to it as NVF (lite).

Tasks. We evaluate the effectiveness of our framework across four distinct reconstruction tasks: 1) category-agnostic, 2) category-unseen, 3) category-specific, and 4) cross-domain. In Section 4.2, we first assess the generalization ability of our NVF (lite) and NVF (ultra) against existing methods through category-agnostic and category-unseen reconstruction. In Section 4.3, we demonstrate the NVF’s capacity for reconstructing non-watertight meshes through category-specific reconstruction. Finally, in Section 4.4, we perform a cross-domain reconstruction test by reconstructing real scanned data without any training or fine-tuning.

Implementations. We follow [76] to use the PointTransformer [87] with $K = 16$ nearest points as our feature encoder and set the grid resolution to 256 for surface extraction. For codebook design, We respectively set the number of heads as 4 and the number of codes and dimensions in each sub-codebook as 256 and 64. During the optimization, we set the learning rate to $l_r = 10^{-4}$ which decays by a factor of 0.3 at steps 30, 70, and 120. Then we apply curl regularization from step 150, with weights λ_{curl} as 10^{-6} and λ_{dir} as 10^{-3} . The Adam optimizer has been utilized for training with a learning rate of 10^{-3} , $(\beta_1, \beta_2) = (0.9, 0.999)$, $\epsilon = 10^{-8}$, and weight decay $\lambda = 0$.

Baseline method implementation. For a fair comparison, we used the publicly released codes of the baseline methods using identical training/testing conditions and the most optimal hyperparameter sets suggested in corresponding papers. We pre-process the shape as DISN [73] and assign sampled query points inside/outside labels according to the codes released by OccNet [45] and IF-Nets [14] for optimizing watertight shape reconstruction. We adopt the same 3D convolution network as the backbone for IF-Nets [14], NDF [15], and GIFs [79]. Their input point clouds are all voxelized with a resolution of 128^3 , consistent with the watertight car reconstruction based on [15], [79]. For non-watertight shape reconstruction, such as category-agnostic, category-unseen, category-specific, and cross-domain reconstructions, the input point clouds of the three aforementioned methods are voxelized with a resolution of 256^3 .

Datasets. We conduct our category-agnostic, category-unseen, and category-specific reconstruction experiments on ShapeNet [8], a large synthetic dataset, whereas we evaluate our model’s generalization ability on MGN [6], a real scanned dataset, through cross-domain reconstruction experiments. All meshes are normalized to a unit cube with a range of $[-0.5, 0.5]$, consistent with existing methods.

ShapeNet is a synthetic dataset with 55 distinct object categories. We use *cars, chairs, planes, and tables* (referred to as *base classes*) categories for category-agnostic reconstruction. We also perform category-unseen reconstruction on the *speakers, bench, lamps, and watercraft* (referred to as the *novel classes*) categories in Tab. 1 and Tab. 2. Last, we use the *cars* category to conduct our category-specific reconstruction experiments in Tab. 3. While, the MGN dataset comprises 5 garment categories, with open surfaces obtained through scanning. We evaluate our framework on MGN to demon-

Methods	Base					Novel				
	CD↓	EMD↓	Normal↓	F1 _{2.5×10⁻⁵} ↑	F1 _{1×10⁻⁴} ↑	CD↓	EMD↓	Normal↓	F1 _{1×10⁻⁵} ↑	F1 _{2×10⁻⁵} ↑
Input	8.398	1.045	N/A	14.148	25.111	7.999	1.024	N/A	17.576	29.815
OccNet [45]	27.658	1.694	0.237	30.877	46.644	447.620	4.013	0.455	15.943	24.433
ConvOccNet [49]	5.479	1.210	0.155	51.872	71.448	17.525	1.669	0.225	44.165	61.417
IF-Net [14]	1.897	1.120	0.098	65.975	85.421	5.961	1.608	0.137	61.670	81.106
NDF [15]	1.689	1.538	0.110	66.802	84.809	1.694	1.741	0.135	65.622	84.069
GIFS [79]	1.793	1.280	0.161	56.188	78.458	1.943	1.534	0.177	56.644	78.016
Ours (lite)	0.910	1.079	0.108	78.503	91.408	1.442	1.145	0.109	80.883	91.836
Ours (ultra)	0.791	1.069	0.079	80.517	92.859	1.361	1.097	0.083	82.622	93.031

TABLE 1: Quantitative results of category-agnostic and category-unseen reconstructions on watertight shapes of ShapeNet. We train all models on the base classes, and evaluate them on the base and the novel classes, respectively.

Methods	Base					Novel				
	CD↓	EMD↓	Normal↓	F1 _{2.5×10⁻⁵} ↑	F1 _{1×10⁻⁴} ↑	CD↓	EMD↓	Normal↓	F1 _{1×10⁻⁵} ↑	F1 _{2×10⁻⁵} ↑
Input	3.170	0.867	N/A	32.875	51.105	2.885	0.843	N/A	39.902	58.092
NDF [15]	0.986	1.372	0.143	72.425	88.754	0.926	1.532	0.171	76.162	89.977
GIFS [79]	1.175	1.260	0.197	64.915	85.115	2.960	1.499	0.230	69.252	86.518
Ours (lite)	0.854	1.197	0.162	75.372	90.266	0.776	1.340	0.169	79.723	91.576
Ours (ultra)	0.810	1.182	0.137	76.256	90.785	0.745	1.309	0.149	80.349	91.897

TABLE 2: Quantitative results of category-agnostic and category-unseen reconstructions on non-watertight shapes of ShapeNet. We train all models on the base classes and evaluate them on the base and the novel classes, respectively.

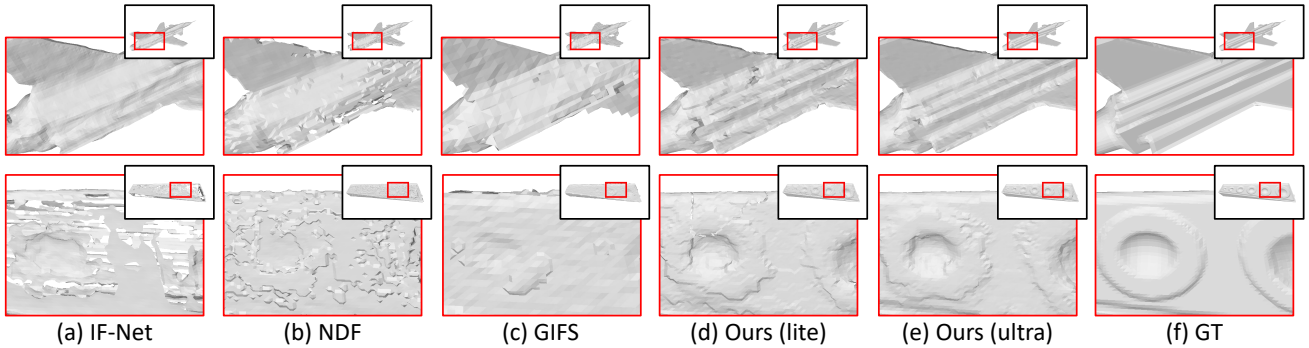


Fig. 6: Visualization of category-agnostic and category-unseen reconstructions on watertight shapes from the ShapeNet dataset. The 1st row, planes, is from the base classes. The 2nd row, speaker, is from the novel classes. We zoom in on part of the shapes (indicated by the red box) to visualize details better.

Methods	CD↓	EMD↓	Normal↓	F1 _{1×10⁻⁵} ↑	F1 _{2×10⁻⁵} ↑
Input	3.631	0.707	N/A	23.735	41.588
NDF [15]	1.971	1.248	0.275	64.116	84.902
GIFS [79]	1.461	0.970	0.302	54.867	79.722
Ours (lite)	1.144	0.945	0.286	64.261	85.290
Ours (ultra)	1.082	0.977	0.244	65.993	86.486

TABLE 3: Quantitative evaluation on ShapeNet Cars. We train and evaluate our method on the raw data of the ShapeNet “Car” category. Our method achieves better performance than the state-of-the-art UDF-based methods.

Methods	CD↓	EMD↓	Normal↓	F1 _{1×10⁻⁵} ↑	F1 _{2×10⁻⁵} ↑
Input	1.243	0.157	N/A	52.189	72.969
NDF [15]	0.252	0.216	0.097	96.338	98.687
GIFS [79]	0.394	0.192	0.128	93.330	97.295
Ours (lite)	0.141	0.184	0.083	98.499	99.498
Ours (ultra)	0.133	0.167	0.070	98.756	99.562

TABLE 4: Quantitative results of cross-domain reconstruction on MGN [6]. We train our models based on ShapeNet with the base classes and evaluate them on the raw data from MGN.

strate our model generalization in the wild.

Data Preprocessing. We generate training point sam-

ples, *i.e.*, query points, along with the corresponding ground-truth displacement vectors. Specifically, we pre-compute 100k points according to the UDF method as in [15]. To capture surface details, we sample points in the vicinity of the surface by randomly selecting a surface point $\hat{\mathbf{q}}$ from the ground-truth mesh, which is displaced by a vector \mathbf{d} drawn from a Gaussian distribution $\mathbf{d} \sim N(0, \Sigma)$. In this way, we can create a 3D query point $\mathbf{q} = \hat{\mathbf{q}} + \mathbf{d}$. We use a diagonal covariance matrix $\Sigma \in \mathbb{R}^{3 \times 3}$ with entries $\Sigma_{i,i} = \sigma$.

During the training stage, we use a subset of 30k samples, where 1% of them generated by $\sigma = 0.08$ for optimizing the displacement predictions for query points far from the surface, 49% generated by $\sigma = 0.02$ for optimizing regression of surface distances within $\sigma = 0.02$, and 50% generated by $\sigma = 0.003$ for optimizing the reconstruction of the detailed surface boundary. We split the training/testing sets as in [76].

Metrics. We adopt Chamfer Distance (CD), Normal Error (Normal), Earth Mover Distance (EMD), and F-score as evaluation metrics. We randomly sample 100k points with their corresponding normals from the reconstructed and ground-truth surfaces to compute CD ($\times 10^{-5}$) and Normal. EMD

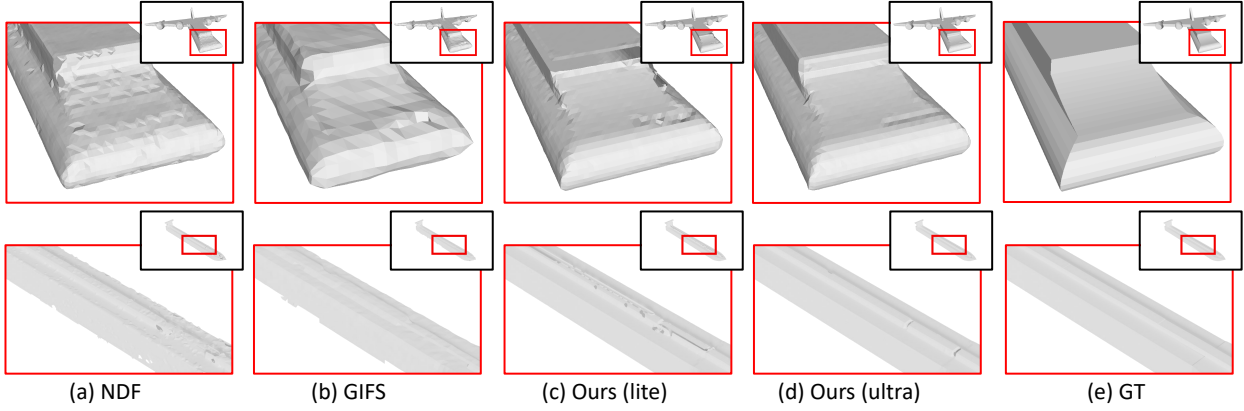


Fig. 7: Visualization of category-agnostic and category-unseen reconstructions on non-watertight shapes from the ShapeNet dataset. The 1st row, airplanes, is from the base classes. The 2nd row, watercraft, are from the novel classes. We zoom in on part of the shapes (indicated by the red box) to visualize details better.

Components	Base					Novel				
	CD↓	EMD↓	Normal↓	F1 _{2.5×10⁻⁵} ↑	F1 _{1×10⁻⁴} ↑	CD↓	EMD↓	Normal↓	F1 _{1×10⁻⁵} ↑	F1 _{2×10⁻⁵} ↑
Vanilla	0.121	1.212	0.196	73.642	88.962	0.081	1.329	0.193	78.800	91.084
+Hard	0.854	1.197	0.162	75.372	90.266	0.776	1.340	0.169	79.723	91.576
+Soft	0.803	1.197	0.143	76.117	90.756	0.818	1.307	0.153	80.254	91.894
+Soft +Curl	0.804	1.190	0.144	76.072	90.718	0.841	1.291	0.153	80.265	91.898
+Soft +Curl +Dir.	0.810	1.182	0.137	76.256	90.785	0.745	1.309	0.149	80.349	91.897

TABLE 5: Quantitative results of alternative NVF (ultra) methods with different proposed components for category-agnostic and category-unseen reconstructions on non-watertight shapes of ShapeNet. We train all models on the base and the novel classes, respectively.

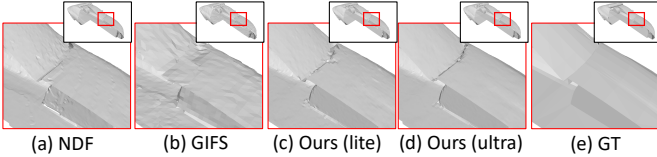


Fig. 8: Qualitative visualization of Category-specific reconstruction on ShapeNet Cars. We zoom in on part of the shape (indicated by the red box) to visualize inner structures better.

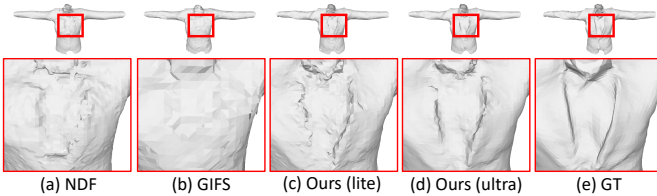


Fig. 9: Visualization of cross-domain reconstruction on the MGN dataset. All models are trained on the base classes of ShapeNet without fine-tuning on MGN. We zoom in on part of the shapes (indicated by the red box) to visualize details better.

($\times 10^{-2}$) is computed using 2048 randomly sampled points and F-score ($\times 10^{-2}$) uses 100,000 points with thresholds 1×10^{-5} and 2×10^{-5} , respectively.

4.2 Category-agnostic and Category-unseen Cases

Watertight shapes. We evaluate the model generalization ability of our NVF through category-agnostic and category-

unseen reconstruction experiments. We report our quantitative experimental results on watertight shapes pre-processed by DISN [73] in Tab. 1 to ensure a fair comparison as previous methods (e.g., OccNet [45] and IF-Net [14]) cannot directly use non-watertight shapes as input. To maintain consistency with IF-Net [14] and NVF [76], we utilize 3k points as input for all methods and adopt the same training/testing split.

We provide quantitative qualitative comparison in Tab. 1 and visualizations of the results in Fig. 6. Thanks to the richer cross-object prior information introduced from the codebook, our NVF (ultra) and NVF (lite) both outperform previous methods. Moreover, NVF (ultra) has better model generalization ability for category-agnostic and category-unseen cases, therefore significantly surpassing UDF-based methods and NVF (lite). The qualitative analysis also demonstrates our method can produce smoother reconstructed surfaces than others due to curl regularization and direction loss. For example, our method can generate intricate details such as the tails of planes or concaves on speakers.

Non-watertight shapes. We also conduct additional experiments on the reconstruction of non-watertight shapes with the same experimental setup as described above. The results are presented in Tab. 2 and Fig. 7. We follow the same data splitting as in NVF [76], where we randomly sample 3000 shapes from each base class for training and 200 shapes from each base and novel class for validation and testing. The input point cloud comprises 10k points sampled from the raw data of the shapes.

As shown in Tab. 2, our methods NVF (ultra) and NVF (lite) outperform all existing methods regarding all matrices.

In particular, NVF (ultra) surpasses the most recent state-of-the-art method on all metrics. In particular, we achieve approximately 5% and 15% normal error reduction on base and novel classes compared with the previous best NDF and GIFS, respectively, which reflecting NVF (ultra) mitigate displacement inaccuracy and reconstruct smoother surfaces. The visualization in Fig. 7 further reveals that NDF, our method produces a smoother reconstructed surface (e.g., the center part for both 1st and 2nd row) with much fewer noises than other methods thanks to introduced curl and direction constraints.

4.3 Category-specific Cases

We present *category-specific reconstruction* using ShapeNet cars, for demonstrating the efficacy in representing a single category. We follow the training/testing set and 10k-point sampling procedure as in [15], [76], [79]. As shown, on this task, our NVF (ultra) outperforms all other methods in comparison, including the second-best performer NVF (lite), over four metrics, including CD, Normal, and two F-scores, while yielding comparable EMD to NVF (lite) and GIFS. Moreover, we demonstrate a qualitative visualization in Fig. 8, where our NVF (ultra) again produces smoother surfaces for finer parts than NDF, GIFS, and NVF (lite).

4.4 Cross-domain Cases

In addition to the above intra-domain reconstruction tasks, we also examine our cross-domain ability. We devised a cross-domain reconstruction experiment and presented quantitative and qualitative results in Tab. 4 and Fig. 9, respectively. Specifically, we assess the performance of our category-agnostic models, which were trained on ShapeNet base classes, on MGN [6] without fine-tuning. We randomly selected 20 shapes from the 5 categories in MGN and used 3,000 points from the raw data as input.

Tab. 4 shows that our proposed NVF (ultra) outperforms other methods in terms of cross-domain reconstruction ability due to the better model generalization brought by a soft codebook than NVF (lite). Specifically, our method significantly reduces approximately 10% and 14% on EMD, and 15% and 45% on normal metrics compared to NVF (lite) and GIFS, respectively. Moreover, the qualitative visualization in Fig. 9 shows that our approach accurately reconstructs the intricate folds and sharp edges of long coats as a better optimization by curl and direction losses, while other methods fail to capture.

5 ANALYSIS

Ablation. We conduct comprehensive ablation studies on non-watertight category-agnostic and category-unseen reconstruction (same settings as Sec. 4.2) to evaluate the effectiveness of the proposed components in Tab. 5, including hard/soft codebook (i.e., hard/soft), curl regularization (i.e., curl) and direction loss (i.e., dir). The results indicate that using codebooks can generally improve the overall performance regarding all metrics, and each introduced component can also improve the overall performance in most metrics.

	Method	Backbone	CD↓	EMD↓	F1 _{1×10⁻⁵} ↑	F1 _{2×10⁻⁵} ↑
Base	NDF [15]	3D Conv	0.99	1.372	72.425	88.754
	Ours (lite)	3D Conv	0.92	1.189	72.415	89.365
		PointTransformer	0.85	1.197	75.372	90.266
	Ours (ultra)	3D Conv	0.886	1.167	73.0827	89.921
PointTransformer		0.810	1.182	76.256	90.785	
Novel	NDF [15]	3D Conv	0.93	1.532	76.162	89.977
	Ours (lite)	3D Conv	0.90	1.342	76.155	90.462
		PointTransformer	0.78	1.340	79.723	91.576
	Ours (ultra)	3D Conv	0.856	1.297	76.781	90.878
PointTransformer		0.745	1.309	80.349	91.897	

TABLE 6: Comparison of different backbones for Ours on non-watertight ShapeNet. The point cloud based backbones outperform the 3D convolution backbone. PointTransformer performs the best. As the soft codebook and curl regularization require more memory, we only apply zero-curl regularization on the efficient backbone, i.e., PointTransformer.

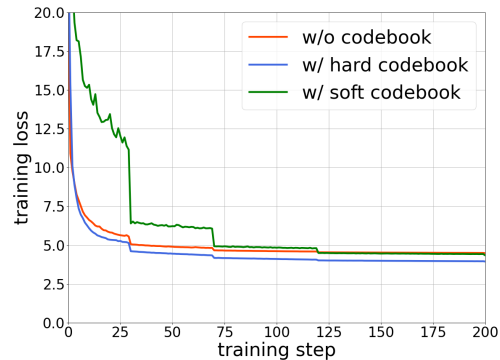


Fig. 10: Training curves of models w/ and w/o codebooks. The models w/ hard codebooks converge faster than those w/o codebook or w/ soft codebook.

Training Effectiveness. We would like to highlight that the introduced “hard” codebook could also work as regularization to reduce the training time. As shown in Fig. 10, the loss curves of the models with (w/) hard codebooks (i.e., blue line) generally converge faster than their corresponding models without (w/o) codebook (i.e., red line) or with (w/) soft codebook (i.e., green line). This observation could be attributed to the incorporation of the *Exponential Moving Average* training strategy introduced by the “hard” codebook, which serves as an additional momentum term and gradient regularizer during optimization. Such a mechanism does not present in the soft codebook and the vanilla version, potentially accounting for their relatively slower convergence than that of the hard codebook.

3D Feature Extraction. We also report our methods with different 3D feature extraction backbones (i.e., 3D convolution [14], [15], [79] and PointTransformer [87]) in Tab. 6. The results show that our NVF can already achieve comparable (if not better) results with NDF using the same extraction backbone (e.g., 3D convolution), while ours is more efficient on runtime and memory cost. Using PointTransformer can consistently improve the overall performance.

Soft vs Hard. The benefits of the soft codebook over the conventional hard one can be seen in Tab. 5 (with the same settings as Sec. 4.2) on nearly all evaluation metrics for both the base and the novel classes, which is consistent with our analysis that the soft codebook enhances the representa-

Methods	Backbone	Runtime	Memory
NDF [15]	3D Conv	0.327s	7.30G
Ours (lite)	PointTransformer	0.113s	2.35G
Ours (ultra)	PointTransformer	0.115s	15.48G

TABLE 7: Inference analysis. The runtime and memory are time cost and peak memory during the inference of 50k queries.

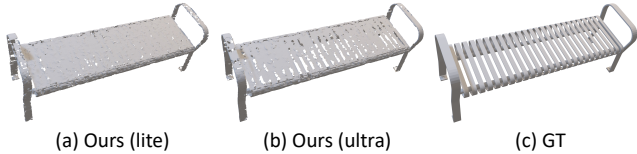


Fig. 11: Visualization of our failure case example, when reconstructing a very thin, complex, and high-frequency 3D structure.

tion ability. Nevertheless, it is important to note that this performance enhancement comes with a trade-off, as the utilization of the soft codebook incurs additional memory requirements compared to the hard one.

Curl Loss. We set a small weight of the curl regularization to balance the magnitudes of different loss terms, and showed two visual examples in the Fig. 5, demonstrating reconstruction results w/o (Fig. 5(c)) and w/ (Fig. 5(d)) using curl regularization. Quantitatively, on non-watertight test objects in ShapeNet, our model produces curl values of 1.256 and 1.404 w/ and w/o using curl regularization for optimization, respectively.

Complexity. We report the inference time and peak GPU memory on the machine with one RTX 3090Ti in Tab. 7 for obtaining the distance and direction of 50k query points. The results show that our NVF (ultra) requires 40% inference time compared with NDF, and an equal level of inference time compared with NDF (lite), while achieving better performance. However, our NVF (ultra) needs more memory compared with NDF and NDF (lite). The underlying reason for this predicament is attributed to the memory overhead associated with the computation of attention maps in the soft codebook. To address this challenge, one possible solution is to adopt a sparse attention mechanism, which would greatly alleviate this computational burden. We aim to investigate and develop such an approach in our forthcoming research endeavors.

Limitations. It is noteworthy that our proposed methodology has the capacity to effectively manage shapes with arbitrary resolution and topology, regardless of whether they are watertight or non-watertight. It is important to acknowledge, however, that there are still certain limitations associated with the reconstruction process, particularly when it comes to very thin, high-frequency, and intricate structures. As evidenced by the example of the bench beam in Fig. 11, there are still areas where the methodology falls short of achieving optimal outcomes.

Explicit Deformation Visualization. In order to demonstrate that NVF could serve as both an implicit neural function and an explicit deformation function (*i.e.*, displacement output of the function could be directly used to deform source meshes), we provide some deformation

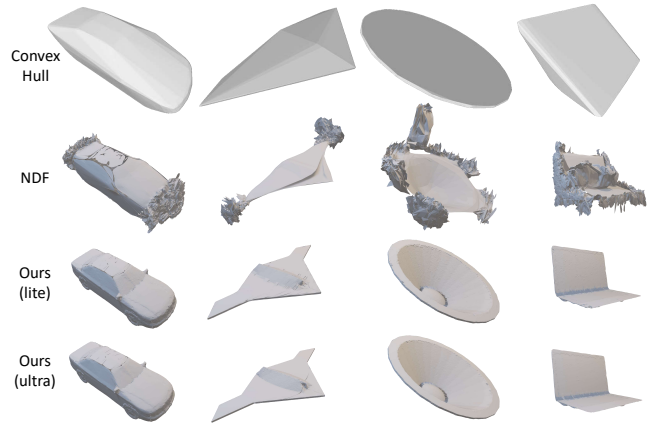


Fig. 12: Mesh deformation visualization. The 1st row represents the source meshes that are the convex hull of the input point clouds, and the 2nd row represents the shapes after deformation by our NVF.

results in Fig. 12, which indicates that our NVF can directly deform the convex hull meshes of the input point cloud to fit the surface.

6 CONCLUSION

In this paper, we present a novel framework for surface reconstruction representation, named Neural Vector Fields (NVFs). Our approach employs hard or soft codebooks to introduce cross-object priors, enriches the feature representation for reconstruction, and enables the differentiability of the framework. Moreover, we propose that the ideal Distance Vector Fields (DVF) should be active and irrotational fields, and we observe that inaccurate displacement predictions lead to uneven surfaces and little holes in reconstructed surfaces. To address this issue, we inject curl regularization and direction loss to better supervise the learning process, leveraging the differentiable soft codebook design which allows for Jacobian matrix calculation. Experimental results demonstrate that our method achieves state-of-the-art reconstruction performance for various topologies.

REFERENCES

- [1] Panos Achlioptas, Olga Diamanti, Ioannis Mitliagkas, and Leonidas J. Guibas. Representation learning and adversarial generation of 3d point clouds. *ArXiv, abs/1707.02392*, 2017. 3
- [2] Eirikur Agustsson, Fabian Mentzer, Michael Tschannen, Lukas Cavigelli, Radu Timofte, Luca Benini, and Luc V Gool. Soft-to-hard vector quantization for end-to-end learning compressible representations. In I. Guyon, U. Von Luxburg, S. Bengio, H. Wallach, R. Fergus, S. Vishwanathan, and R. Garnett, editors, *Advances in Neural Information Processing Systems*, volume 30. Curran Associates, Inc., 2017. 3
- [3] Abhishek Badki, Orazio Gallo, Jan Kautz, and Pradeep Sen. Meshlet priors for 3d mesh reconstruction. *2020 IEEE/CVF Conference on Computer Vision and Pattern Recognition (CVPR)*, Jun 2020. 1
- [4] Jan Bednarik, Shaifali Parashar, Erhan Gundogdu, Mathieu Salzmann, and Pascal Fua. Shape reconstruction by learning differentiable surface representations. *2020 IEEE/CVF Conference on Computer Vision and Pattern Recognition (CVPR)*, Jun 2020. 1
- [5] F. Bernardini, J. Mittleman, H. Rushmeier, C. Silva, and G. Taubin. The ball-pivoting algorithm for surface reconstruction. *IEEE Transactions on Visualization and Computer Graphics*, 5(4):349–359, 1999. 1, 3

- [6] Bharat Lal Bhatnagar, Garvita Tiwari, Christian Theobalt, and Gerard Pons-Moll. Multi-garment net: Learning to dress 3d people from images. In *IEEE International Conference on Computer Vision (ICCV)*. IEEE, Oct 2019. [2, 7, 8, 10](#)
- [7] Edwin Catmull and James Clark. Recursively generated b-spline surfaces on arbitrary topological meshes. *Computer-aided design*, 10(6):350–355, 1978. [1](#)
- [8] Angel X Chang, Thomas Funkhouser, Leonidas Guibas, Pat Hanrahan, Qixing Huang, Zimo Li, Silvio Savarese, Manolis Savva, Shuran Song, Hao Su, et al. Shapenet: An information-rich 3d model repository. *arXiv preprint arXiv:1512.03012*, 2015. [2, 7](#)
- [9] R. Qi Charles, Hao Su, Mo Kaichun, and Leonidas J. Guibas. Pointnet: Deep learning on point sets for 3d classification and segmentation. *2017 IEEE Conference on Computer Vision and Pattern Recognition (CVPR)*, Jul 2017. [3](#)
- [10] Jiawen Chen, Dennis Bautembach, and Shahram Izadi. Scalable real-time volumetric surface reconstruction. *ACM Trans. Graph.*, 32(4), jul 2013. [1, 3](#)
- [11] Ting Chen and Yizhou Sun. Differentiable product quantization for end-to-end embedding compression. In *ICML*, 2020. [3](#)
- [12] Zhiqin Chen and Hao Zhang. Learning implicit fields for generative shape modeling. *2019 IEEE/CVF Conference on Computer Vision and Pattern Recognition (CVPR)*, Jun 2019. [1, 3](#)
- [13] An-Chieh Cheng, Xueting Li, Sifei Liu, Min Sun, and Ming-Hsuan Yang. Autoregressive 3d shape generation via canonical mapping. In *ECCV*, 2022. [3](#)
- [14] Julian Chibane, Thiemo Alldieck, and Gerard Pons-Moll. Implicit functions in feature space for 3d shape reconstruction and completion. *2020 IEEE/CVF Conference on Computer Vision and Pattern Recognition (CVPR)*, Jun 2020. [1, 3, 7, 8, 9, 10](#)
- [15] Julian Chibane, Aymen Mir, and Gerard Pons-Moll. Neural unsigned distance fields for implicit function learning. In *Advances in Neural Information Processing Systems (NeurIPS)*, December 2020. [1, 3, 7, 8, 10, 11](#)
- [16] Christopher Choy, JunYoung Gwak, and Silvio Savarese. 4d spatio-temporal convnets: Minkowski convolutional neural networks. In *2019 IEEE/CVF Conference on Computer Vision and Pattern Recognition (CVPR)*, pages 3070–3079, 2019. [3](#)
- [17] Christopher B Choy, Danfei Xu, JunYoung Gwak, Kevin Chen, and Silvio Savarese. 3d-r2n2: A unified approach for single and multi-view 3d object reconstruction. In *European conference on computer vision*, pages 628–644. Springer, 2016. [3](#)
- [18] Boyang Deng, J. P. Lewis, Timothy Jeruzalski, Gerard Pons-Moll, Geoffrey Hinton, Mohammad Norouzi, and Andrea Tagliasacchi. Nasa neural articulated shape approximation. *Lecture Notes in Computer Science*, page 612–628, 2020. [3](#)
- [19] Theo Deprelle, Thibault Groueix, Matthew Fisher, Vladimir Kim, Bryan Russell, and Mathieu Aubry. Learning elementary structures for 3d shape generation and matching. In *Advances in Neural Information Processing Systems*, pages 7433–7443, 2019. [1](#)
- [20] Prafulla Dhariwal, Heewoo Jun, Christine Payne, Jong Wook Kim, Alec Radford, and Ilya Sutskever. Jukebox: A generative model for music. *arXiv preprint arXiv:2005.00341*, 2020. [3](#)
- [21] Ming Ding, Zhuoyi Yang, Wenyi Hong, Wendi Zheng, Chang Zhou, Da Yin, Junyang Lin, Xu Zou, Zhou Shao, Hongxia Yang, and Jie Tang. Cogview: Mastering text-to-image generation via transformers. In *NeurIPS*, 2021. [3](#)
- [22] Philipp Erler, Paul Guerrero, Stefan Ohrhallinger, Niloy J. Mitra, and Michael Wimmer. Points2Surf: Learning implicit surfaces from point clouds. In Andrea Vedaldi, Horst Bischof, Thomas Brox, and Jan-Michael Frahm, editors, *Computer Vision – ECCV 2020*, pages 108–124, Cham, 2020. Springer International Publishing. [1](#)
- [23] Songwei Ge, Thomas Hayes, Harry Yang, Xiaoyue Yin, Guan Pang, David Jacobs, Jia-Bin Huang, and Devi Parikh. Long video generation with time-agnostic vqgan and time-sensitive transformer. In *ECCV*, 2022. [3](#)
- [24] Kyle Genova, Forrester Cole, Avneesh Sud, Aaron Sarna, and Thomas Funkhouser. Local deep implicit functions for 3d shape. In *2020 IEEE Conference on Computer Vision and Pattern Recognition (CVPR)*, 2019. [3](#)
- [25] Georgia Gkioxari, Jitendra Malik, and Justin Johnson. Mesh r-cnn. In *Proceedings of the IEEE/CVF International Conference on Computer Vision*, pages 9785–9795, 2019. [3](#)
- [26] Thibault Groueix, Matthew Fisher, Vladimir G Kim, Bryan C Russell, and Mathieu Aubry. A papier-mâché approach to learning 3d surface generation. In *Proceedings of the IEEE conference on computer vision and pattern recognition*, pages 216–224, 2018. [1, 3](#)
- [27] Shuyang Gu, Dong Chen, Jianmin Bao, Fang Wen, Bo Zhang, Dongdong Chen, Lu Yuan, and Baining Guo. Vector quantized diffusion model for text-to-image synthesis. *2022 IEEE/CVF Conference on Computer Vision and Pattern Recognition (CVPR)*, pages 10686–10696, 2022. [3](#)
- [28] Benoit Guillard, Federico Stella, and Pascal Fua. Meshudf: Fast and differentiable meshing of unsigned distance field networks. *arXiv preprint arXiv:2111.14549*, 2021. [1, 3, 7](#)
- [29] Kunal Gupta and Manmohan Chandraker. Neural mesh flow: 3d manifold mesh generation via diffeomorphic flows. In *Advances in Neural Information Processing Systems*, volume abs/2007.10973, 2020. [1](#)
- [30] Christian Hane, Shubham Tulsiani, and Jitendra Malik. Hierarchical surface prediction for 3d object reconstruction. *2017 International Conference on 3D Vision (3DV)*, Oct 2017. [1, 3](#)
- [31] Wenyi Hong, Ming Ding, Wendi Zheng, Xinghan Liu, and Jie Tang. Cogvideo: Large-scale pretraining for text-to-video generation via transformers, 2022. [3](#)
- [32] Qingyong Hu, Bo Yang, Linhai Xie, Stefano Rosa, Yulan Guo, Zhihua Wang, Niki Trigoni, and Andrew Markham. Randalnet: Efficient semantic segmentation of large-scale point clouds. *2020 IEEE/CVF Conference on Computer Vision and Pattern Recognition (CVPR)*, Jun 2020. [3](#)
- [33] Binh-Son Hua, Minh-Khoi Tran, and Sai-Kit Yeung. Pointwise convolutional neural networks. In *Proceedings of the IEEE conference on computer vision and pattern recognition*, pages 984–993, 2018. [3](#)
- [34] Mengqi Ji, Juergen Gall, Haitian Zheng, Yebin Liu, and Lu Fang. SurfacerNet: An end-to-end 3d neural network for multiview stereopsis. In *Proceedings of the IEEE International Conference on Computer Vision (ICCV)*, pages 2307–2315, 2017. [3](#)
- [35] Chiyu Jiang, Avneesh Sud, Ameesh Makadia, Jingwei Huang, Matthias Nießner, and Thomas Funkhouser. Local implicit grid representations for 3d scenes. *2020 IEEE/CVF Conference on Computer Vision and Pattern Recognition (CVPR)*, Jun 2020. [1, 3](#)
- [36] Angjoo Kanazawa, Shubham Tulsiani, Alexei A. Efros, and Jitendra Malik. Learning category-specific mesh reconstruction from image collections. *Lecture Notes in Computer Science*, page 386–402, 2018. [3](#)
- [37] Abhishek Kar, Christian Häne, and Jitendra Malik. Learning a multi-view stereo machine. In *NeurIPS*. 2017. [3](#)
- [38] Michael Kazhdan, Matthew Bolitho, and Hugues Hoppe. Poisson surface reconstruction. In *Proceedings of the fourth Eurographics symposium on Geometry processing*, volume 7, 2006. [1](#)
- [39] Doyup Lee, Chiheon Kim, Saehoon Kim, Minsu Cho, and Wook-Shin Han. Autoregressive image generation using residual quantization. *2022 IEEE/CVF Conference on Computer Vision and Pattern Recognition (CVPR)*, Jun 2022. [3](#)
- [40] Jiabao Lei, Kui Jia, and Yi Ma. Learning and meshing from deep implicit surface networks using an efficient implementation of analytic marching. *IEEE Transactions on Pattern Analysis and Machine Intelligence*, 44(12):10068–10086, 2022. [1](#)
- [41] Chen-Hsuan Lin, Oliver Wang, Bryan C. Russell, Eli Shechtman, Vladimir G. Kim, Matthew Fisher, and Simon Lucey. Photometric mesh optimization for video-aligned 3d object reconstruction. *2019 IEEE/CVF Conference on Computer Vision and Pattern Recognition (CVPR)*, Jun 2019. [3](#)
- [42] Yongcheng Liu, Bin Fan, Shiming Xiang, and Chunhong Pan. Relation-shape convolutional neural network for point cloud analysis. *2019 IEEE/CVF Conference on Computer Vision and Pattern Recognition (CVPR)*, Jun 2019. [3](#)
- [43] William E. Lorensen and Harvey E. Cline. Marching cubes: A high resolution 3d surface construction algorithm. *SIGGRAPH Comput. Graph.*, 21(4):163–169, aug 1987. [1, 7](#)
- [44] Daniel Maturana and Sebastian Scherer. Voxnet: A 3d convolutional neural network for real-time object recognition. In *IEEE/RSJ International Conference on Intelligent Robots and Systems*, pages 922–928, 2015. [3](#)
- [45] Lars Mescheder, Michael Oechsle, Michael Niemeyer, Sebastian Nowozin, and Andreas Geiger. Occupancy networks: Learning 3d reconstruction in function space. In *Proceedings IEEE Conf. on Computer Vision and Pattern Recognition (CVPR)*, 2019. [1, 3, 7, 8, 9](#)
- [46] Paritosh Mittal, Yen-Chi Cheng, Maneesh Singh, and Shubham Tulsiani. Autosdf: Shape priors for 3d completion, reconstruction and generation. *2022 IEEE/CVF Conference on Computer Vision and Pattern Recognition (CVPR)*, Jun 2022. [3](#)
- [47] Junyi Pan, Xiaoguang Han, Weikai Chen, Jiapeng Tang, and Kui Jia. Deep mesh reconstruction from single rgb images via topology

- modification networks. 2019 IEEE/CVF International Conference on Computer Vision (ICCV), Oct 2019. [3](#)
- [48] Jeong Joon Park, Peter Florence, Julian Straub, Richard Newcombe, and Steven Lovegrove. DeepSDF: Learning continuous signed distance functions for shape representation. 2019 IEEE/CVF Conference on Computer Vision and Pattern Recognition (CVPR), Jun 2019. [3](#)
- [49] Songyou Peng, Michael Niemeyer, Lars Mescheder, Marc Pollefeys, and Andreas Geiger. Convolutional occupancy networks. In European Conference on Computer Vision (ECCV), 2020. [1, 8](#)
- [50] Charles Ruizhongtai Qi, Li Yi, Hao Su, and Leonidas J Guibas. Pointnet++: Deep hierarchical feature learning on point sets in a metric space. *Advances in neural information processing systems*, 30, 2017. [3](#)
- [51] Anurag Ranjan, Timo Bolkart, Soubhik Sanyal, and Michael J. Black. Generating 3d faces using convolutional mesh autoencoders. *Lecture Notes in Computer Science*, page 725–741, 2018. [3](#)
- [52] Ali Razavi, Aaron van den Oord, and Oriol Vinyals. Generating Diverse High-Fidelity Images with VQ-VAE-2. Curran Associates Inc., Red Hook, NY, USA, 2019. [3](#)
- [53] Jingjing Ren, Qingqing Zheng, Yuan yu Zhao, Xuemiao Xu, and Chen Li. DFormer: Discrete latent transformer for video inpainting. 2022 IEEE/CVF Conference on Computer Vision and Pattern Recognition (CVPR), pages 3501–3510, 2022. [3](#)
- [54] Danilo Jimenez Rezende, S. M. Ali Eslami, Shakir Mohamed, Peter W. Battaglia, Max Jaderberg, and Nicolas Manfred Otto Heess. Unsupervised learning of 3d structure from images. In NIPS, 2016. [3](#)
- [55] Gernot Riegler, Ali Osman Ulusoy, and Andreas Geiger. Octnet: Learning deep 3d representations at high resolutions. 2017 IEEE Conference on Computer Vision and Pattern Recognition (CVPR), Jul 2017. [3](#)
- [56] Shunsuke Saito, Zeng Huang, Ryota Natsume, Shigeo Morishima, Hao Li, and Angjoo Kanazawa. Pifu: Pixel-aligned implicit function for high-resolution clothed human digitization. 2019 IEEE/CVF International Conference on Computer Vision (ICCV), Oct 2019. [3](#)
- [57] Shunsuke Saito, Tomas Simon, Jason Saragih, and Hanbyul Joo. Pifuhd: Multi-level pixel-aligned implicit function for high-resolution 3d human digitization. In Proceedings of the IEEE Conference on Computer Vision and Pattern Recognition, June 2020. [3](#)
- [58] Frank Steinbrücker, Jürgen Sturm, and Daniel Cremers. Volumetric 3d mapping in real-time on a cpu. In 2014 IEEE International Conference on Robotics and Automation (ICRA), pages 2021–2028, 2014. [3](#)
- [59] Xingyuan Sun, Jiajun Wu, Xiuming Zhang, Zhoutong Zhang, Chengkai Zhang, Tianfan Xue, Joshua B Tenenbaum, and William T Freeman. Pix3d: Dataset and methods for single-image 3d shape modeling. In IEEE Conference on Computer Vision and Pattern Recognition (CVPR), 2018. [3](#)
- [60] Jiapeng Tang, Xiaoguang Han, Mingkui Tan, Xin Tong, and Kui Jia. Skeletonet: A topology-preserving solution for learning mesh reconstruction of object surfaces from rgb images. *IEEE Transactions on Pattern Analysis and Machine Intelligence*, 44(10):6454–6471, 2022. [1](#)
- [61] Maxim Tatarchenko, Alexey Dosovitskiy, and Thomas Brox. Octree generating networks: Efficient convolutional architectures for high-resolution 3d outputs. 2017 IEEE International Conference on Computer Vision (ICCV), Oct 2017. [1, 3](#)
- [62] Hugues Thomas, Charles R. Qi, Jean-Emmanuel Deschaud, Beatriz MarcoteGui, Francois Goulette, and Leonidas Guibas. Kpconv: Flexible and deformable convolution for point clouds. 2019 IEEE/CVF International Conference on Computer Vision (ICCV), Oct 2019. [3](#)
- [63] Aaron van den Oord, Oriol Vinyals, and Koray Kavukcuoglu. Neural discrete representation learning. In NIPS, 2017. [3, 5](#)
- [64] Rahul Venkatesh, Tejan Karmali, Sarthak Sharma, Aurobrata Ghosh, R. Venkatesh Babu, Laszlo A. Jeni, and Maneesh Singh. Deep implicit surface point prediction networks. 2021 IEEE/CVF International Conference on Computer Vision (ICCV), Oct 2021. [3](#)
- [65] Jacob Walker, Ali Kazavi, and Aaron van den Oord. Predicting video with vqvae. *ArXiv*, abs/2103.01950, 2021. [3](#)
- [66] Bing Wang, Zhengdi Yu, Bo Yang, Jie Qin, Toby Breckon, Ling Shao, Niki Trigoni, and Andrew Markham. Rangeudf: Semantic surface reconstruction from 3d point clouds, 2022. [3](#)
- [67] Nanyang Wang, Yinda Zhang, Zhuwen Li, Yanwei Fu, Wei Liu, and Yu-Gang Jiang. Pixel2mesh: Generating 3d mesh models from single rgb images. In Proceedings of the European Conference on Computer Vision (ECCV), pages 52–67, 2018. [3](#)
- [68] Shenlong Wang, Simon Suo, Wei-Chiu Ma, Andrei Pokrovsky, and Raquel Urtasun. Deep parametric continuous convolutional neural networks. 2018 IEEE/CVF Conference on Computer Vision and Pattern Recognition, Jun 2018. [3](#)
- [69] Yue Wang, Yongbin Sun, Ziwei Liu, Sanjay E. Sarma, Michael M. Bronstein, and Justin M. Solomon. Dynamic graph cnn for learning on point clouds. *ACM Transactions on Graphics*, 38(5):1–12, Nov 2019. [3](#)
- [70] Francis Williams, Teseo Schneider, Claudio Silva, Denis Zorin, Joan Bruna, and Daniele Panozzo. Deep geometric prior for surface reconstruction. 2019 IEEE/CVF Conference on Computer Vision and Pattern Recognition (CVPR), Jun 2019. [1](#)
- [71] Jiajun Wu, Yifan Wang, Tianfan Xue, Xingyuan Sun, William T Freeman, and Joshua B Tenenbaum. MarrNet: 3D Shape Reconstruction via 2.5D Sketches. In *Advances In Neural Information Processing Systems*, 2017. [3](#)
- [72] Jiajun Wu, Chengkai Zhang, Tianfan Xue, Bill Freeman, and Joshua B. Tenenbaum. Learning a probabilistic latent space of object shapes via 3d generative-adversarial modeling. In NIPS, 2016. [3](#)
- [73] Qiangeng Xu, Weiyue Wang, Duygu Ceylan, Radomir Mech, and Ulrich Neumann. Disn: Deep implicit surface network for high-quality single-view 3d reconstruction. In H. Wallach, H. Larochelle, A. Beygelzimer, F. d’Alché-Buc, E. Fox, and R. Garnett, editors, *Advances in Neural Information Processing Systems 32*, pages 492–502. Curran Associates, Inc., 2019. [7, 9](#)
- [74] Xingguang Yan, Liqiang Lin, Niloy J. Mitra, Dani Lischinski, Danny Cohen-Or, and Hui Huang. Shapeformer: Transformer-based shape completion via sparse representation, 2022. [3](#)
- [75] Karren Yang, Dejan Markovic, Steven Krenn, Vasu Agrawal, and Alexander Richard. Audio-visual speech codecs: Rethinking audio-visual speech enhancement by re-synthesis. 2022 IEEE/CVF Conference on Computer Vision and Pattern Recognition (CVPR), Jun 2022. [3](#)
- [76] Xianghui Yang, Guosheng Lin, Zhenghao Chen, and Luping Zhou. Neural vector fields: Implicit representation by explicit learning. In 2023 IEEE/CVF Conference on Computer Vision and Pattern Recognition (CVPR). IEEE, Jun 2023. [2, 3, 7, 8, 9, 10](#)
- [77] Xianghui Yang, Guosheng Lin, and Luping Zhou. Single-view 3d mesh reconstruction for seen and unseen categories. *IEEE Transactions on Image Processing*, 32:3746–3758, 2023. [3](#)
- [78] Yaoqing Yang, Chen Feng, Yiru Shen, and Dong Tian. Foldingnet: Interpretable unsupervised learning on 3d point clouds. 2018 IEEE/CVF Conference on Computer Vision and Pattern Recognition, abs/1712.07262, 2017. [3](#)
- [79] Jianglong Ye, Yuntao Chen, Naiyan Wang, and Xiaolong Wang. Gifs: Neural implicit function for general shape representation. In Proceedings of the IEEE/CVF Conference on Computer Vision and Pattern Recognition, 2022. [1, 3, 7, 8, 10](#)
- [80] Fukun Yin, Wen Liu, Zilong Huang, Pei Cheng, Tao Chen, and Gang YU. Coordinates are not lonely—codebook prior helps implicit neural 3d representations. In *Advances in Neural Information Processing Systems (NeurIPS)*, 2022. [3](#)
- [81] Jiahui Yu, Xin Li, Jing Yu Koh, Han Zhang, Ruoming Pang, James Qin, Alexander Ku, Yuanzhong Xu, Jason Baldridge, and Yonghui Wu. Vector-quantized image modeling with improved vqgan. *ICLR*, abs/2110.04627, 2022. [3](#)
- [82] Wentao Yuan, Tejas Khot, David Held, Christoph Mertz, and Martial Hebert. Pcn: Point completion network. 2018 International Conference on 3D Vision (3DV), Sep 2018. [3](#)
- [83] Manzil Zaheer, Satwik Kottur, Siamak Ravanbakhsh, Barnabás Póczos, Ruslan Salakhutdinov, and Alex Smola. Deep sets. *Advances in neural information processing systems*, abs/1703.06114, 2017. [3](#)
- [84] Biao Zhang, Matthias Nießner, and Peter Wonka. 3dilig: Irregular latent grids for 3d generative modeling. *NIPS*, abs/2205.13914, 2022. [3](#)
- [85] Biao Zhang, Jiapeng Tang, Matthias Niessner, and Peter Wonka. 3dshape2vecset: A 3d shape representation for neural fields and generative diffusion models, 2023. [3](#)
- [86] Fang Zhao, Wenhao Wang, Shengcai Liao, and Ling Shao. Learning anchored unsigned distance functions with gradient direction alignment for single-view garment reconstruction. In Proceedings of the IEEE/CVF International Conference on Computer Vision, pages 12674–12683, 2021. [3](#)
- [87] Hengshuang Zhao, Li Jiang, Jiaya Jia, Philip Torr, and Vladlen Koltun. Point transformer. 2021 IEEE/CVF International Conference on Computer Vision (ICCV), Oct 2021. [3, 7, 10](#)
- [88] Tianchen Zhao, Niansong Zhang, Xuifei Ning, He Wang, Li Yi,

- and Yu Wang. Codedvtr: Codebook-based sparse voxel transformer with geometric guidance. In Proceedings of the IEEE/CVF Conference on Computer Vision and Pattern Recognition, pages 1435–1444, 2022. [3](#)
- [89] Junsheng Zhou, Baorui Ma, Liu Yu-Shen, Fang Yi, and Han Zhizhong. Learning consistency-aware unsigned distance functions progressively from raw point clouds. In Advances in Neural Information Processing Systems (NeurIPS), 2022. [1](#), [3](#), [7](#)
- [90] Yin Zhou and Oncel Tuzel. Voxelnet: End-to-end learning for point cloud based 3d object detection. 2018 IEEE/CVF Conference on Computer Vision and Pattern Recognition, Jun 2018. [3](#)